

3-1-2012

# The response of Black Rapids Glacier, Alaska, to the Denali earthquake rock avalanches

Dan H. Shugar

Bernhard T. Rabus

John J. Clague

Denny M. Capps

Follow this and additional works at: [https://digitalcommons.tacoma.uw.edu/ias\\_pub](https://digitalcommons.tacoma.uw.edu/ias_pub)

---

## Recommended Citation

Shugar, Dan H.; Rabus, Bernhard T.; Clague, John J.; and Capps, Denny M., "The response of Black Rapids Glacier, Alaska, to the Denali earthquake rock avalanches" (2012). *SIAS Faculty Publications*. 337.  
[https://digitalcommons.tacoma.uw.edu/ias\\_pub/337](https://digitalcommons.tacoma.uw.edu/ias_pub/337)

This Article is brought to you for free and open access by the School of Interdisciplinary Arts and Sciences at UW Tacoma Digital Commons. It has been accepted for inclusion in SIAS Faculty Publications by an authorized administrator of UW Tacoma Digital Commons.



## 34 1 INTRODUCTION

35 Large landslides can impact glaciers in many ways, notably by changing ice surface topography,  
36 glacier hydrology, albedo, stress state and ice velocity. Several authors have investigated the effects of  
37 large landslide debris sheets on glacier mass balance [e.g. *Bull and Marangunic*, 1967, 1968; *Deline*,  
38 2005; *Reznichenko et al.*, 2010; *Vacco et al.*, 2010; *Reznichenko et al.*, 2011] or on subglacial and  
39 englacial drainage [*Reynolds*, 2000; *Gulley and Benn*, 2007]. Others have examined the effect of  
40 changing ice surface elevation on hydraulic potential [*Fountain and Vaughan*, 1995; *Fischer et al.*,  
41 2005]. Few authors however, have attempted to quantify the effects of landslide debris on glacier flow,  
42 partly because pre-landslide velocity measurements are rarely available. Some researchers, however,  
43 have reported significant changes in glacier dynamics, including advances or surges, following large  
44 landslides [*Tarr*, 1910; *Gardner and Hewitt*, 1990; *Deline*, 2005].

45 Recent studies suggest that large landslides are more common in glacierized mountains than  
46 previously thought [*Geertsema et al.*, 2006]. Ice velocity data for glaciers that have experienced rock  
47 avalanches, however, are rare. *Bull and Marangunic* [1968] attributed an ~10% increase in surface  
48 velocity of Sherman Glacier to the 1964 rock avalanche, based on a local velocity anomaly, but without  
49 pre-landslide measurements. During fieldwork in 2008, we observed that Sherman Glacier was  
50 advancing. *Gardner and Hewitt* [1990] attributed the 1987 and 1989 surges of Bualtar Glacier in  
51 Pakistan to three landslides in 1986, and M. Truffer (unpublished data, 2006; available at  
52 <http://www.gi.alaska.edu/~truffer/>) documented a 2006 surge of McGinnis Glacier, most of which was  
53 covered by debris of two rock avalanches triggered by the 2002 Denali earthquake. *Shulmeister et al.*  
54 [2009] provided a simple theoretical model for acceleration of a glacier following emplacement of a  
55 rock avalanche debris sheet, but were unable to validate the model with field data.

56 The objective of this study is to quantify and understand the response of Black Rapids Glacier to  
57 three rock avalanches triggered by the Denali earthquake in 2002. We compare pre- and post-landslide

58 ice velocities derived from space-borne radar satellite data and ground survey measurements, and use a  
59 full-Stokes ice-flow model to try to explain the observed changes in the velocity field.

## 60 **2 SETTING**

61 Black Rapids Glacier is a 40-km long, surge-type valley glacier in the eastern Alaska Range of  
62 interior Alaska (Figure 1). The glacier last surged in 1936-1937 [*Hance, 1937*] and has been extensively  
63 studied since then [*Péwé, 1951; Post, 1960; Harrison et al., 1975; Heinrichs et al., 1996; Truffer et al.,*  
64 *1999; Rabus and Fatland, 2000; Truffer et al., 2001; Nolan, 2003; Amundson et al., 2006; Shugar et al.,*  
65 *2010; Shugar and Clague, in press*].

66 The  $M_w 7.9$  Denali Fault earthquake, which occurred on 3 November 2002, triggered many  
67 landslides across the Alaska Range, including three large rock avalanches on Black Rapids Glacier  
68 (BRG-west, BRG-middle, and BRG-east; Figure 1). The landslides provide an opportunity to study the  
69 ice dynamics response to the instantaneous emplacement of  $\sim 30 \times 10^6 \text{ m}^3$  of debris over  $\sim 11 \text{ km}^2$  of the  
70 glacier's ablation zone [*Shugar and Clague, in press*]. Black Rapids Glacier, however, presents  
71 challenges for such a study, because of its spatially and temporally complex velocity field [*Nolan, 2003*]  
72 and difficulties in applying radar remote sensing methods to temperate glaciers [e.g. *Massom and Lubin,*  
73 *2006*].

74 Since it was first surveyed in 1973, the surface velocity of Black Rapids Glacier has oscillated, with  
75 a period of approximately 12 years [*Heinrichs et al., 1996*]. The pattern and timing of these oscillations  
76 are consistent at km 20 and km 14, suggesting strong longitudinal stress coupling in the middle reach of  
77 the glacier [*Nolan, 2003*]. *Heinrichs et al. [1996]* attributed these flow variations to changes in basal  
78 motion rather than ice deformation. The decadal-scale oscillations on the upper half of the glacier have  
79 been large – more than 50% in the case of the km 8 and km 14 survey stations [*Truffer et al., 2005*]. No  
80 significant decadal velocity cycles have been observed below km 20, although survey data on the lower  
81 half of the glacier are limited. The difference in flow between the upper and lower parts of the glacier

82 may be due to different basal conditions, or to an effect on stress coupling by the Locket tributary, which  
83 joins the main trunk of Black Rapids Glacier near km 24 (Figure 1).

84 Black Rapids Glacier also exhibits strong seasonal velocity fluctuations, with a peak in June and  
85 much lower and generally less variable velocities in winter (October – February) [Heinrichs *et al.*, 1996;  
86 Rabus and Fatland, 2000]. Survey stations that exhibit marked seasonal speed variations (km 14, 20, 26,  
87 and 32) lie on or near the Denali Fault. Three of these sites (km 14, 20, and 32) have also experienced  
88 large long-term changes in annual velocity and are located in the ablation area [Heinrichs *et al.*, 1996]. It  
89 is not presently known if or how the Denali Fault influences these stations.

### 90 **3 DATA AND METHODS**

91 We generated pre-landslide glacier velocity maps using interferometric synthetic aperture radar  
92 (InSAR), and post-landslide velocity maps using SAR speckle tracking. We then compared the satellite  
93 data with ground-based survey measurements made since the 1970s and numerical model results of  
94 glacier dynamics to examine if changes observed with SAR are characteristic features of post-landslide  
95 glacier flow. A network of survey stations was established along the centerline of the glacier in 1973  
96 [Heinrichs *et al.*, 1995], and each station was denoted by its distance from the head of the glacier; for  
97 example, survey station “km 26” is located 26 km from the head of the glacier (Figure 1). Table 1  
98 provides a summary of all satellite data used in the study.

99 Data limitations constrained our choice of analytical techniques. We were able to perform  
100 conventional interferometric processing with pre-landslide SAR data, but post-landslide SAR data were  
101 decorrelated (see below), especially over bare glacier ice. As a result, we used SAR speckle tracking for  
102 post-landslide velocity calculations.

#### 103 **3.1 Interferometric velocity measurements**

104 Interferograms were generated from ERS-1/2 tandem data. The topographic signal was removed  
105 using the 30-m DEM of the 1995 surface of Black Rapids Glacier produced by Shugar *et al.* [2010].

106 Atmospheric errors were filtered manually by masking glacierized areas and creating a smooth  
107 atmospheric screen, which was then subtracted from the interferogram.

108 Our approach differs from the similar method used by *Mohr et al.* [2003], in that we do not assume  
109 surface-parallel flow, but rather use flow direction vectors constrained by flow features and valley walls  
110 [*Lang et al.*, 2004]. We digitized about 520 flow direction vectors in ArcGIS using a geocoded 2000  
111 Landsat image of the glacier. These discrete vectors represent long-term averages of flow. We checked  
112 their accuracy by plotting long-term survey velocity vectors, based on data from *Heinrichs et al.* [1996]  
113 and M. Truffer (personal communication, May 2011). The digitized vectors were then interpolated to a  
114 regular grid using a Delauney triangulation to produce flow direction vectors parallel to the glacier  
115 surface for every pixel of the glacier [see *Rabus and Lang*, 2000]. In this manner, we were able to  
116 compute complete fields of surface parallel and surface normal (emergence) velocity. An assumption in  
117 this analysis, however, is that flow is invariant between image acquisitions. In the present study, the  
118 images were acquired only days apart (e.g. Table 1), and so this assumption is most likely valid.

119 Instead of using the Cartesian coordinate system ( $X, Y, Z$ ) [*Joughin et al.*, 1998], we rotated the flow  
120 field into a system with axes oriented parallel ( $II$ ), vertically perpendicular ( $\perp$ ), and horizontally  
121 transverse ( $t$ ) to the glacier flow direction. The perpendicular component of velocity is nearly vertical,  
122 because Black Rapids Glacier has a very low surface gradient. The velocity,  $v$ , and the direction vectors,  
123  $\eta$ , use this same notation:

$$124 \quad v = v_{II}\eta_{II} + v_{\perp}\eta_{\perp} + v_t\eta_t \quad (1)$$

125 Assuming the transverse velocity,  $v_{\perp}$ , is zero, velocities in the satellite line-of-sight direction (LOS) for  
126 the ascending ( $A$ ) and descending ( $D$ ) passes, are:

$$127 \quad v^{(A)} = v \cdot \eta_{LOS}^{(A)} = v_{II} \left( \eta_{II} \cdot \eta_{LOS}^{(A)} \right) + v_{\perp} \left( \eta_{\perp} \cdot \eta_{LOS}^{(A)} \right) \quad (2a)$$

$$128 \quad v^{(D)} = v \cdot \eta_{LOS}^{(D)} = v_{II} \left( \eta_{II} \cdot \eta_{LOS}^{(D)} \right) + v_{\perp} \left( \eta_{\perp} \cdot \eta_{LOS}^{(D)} \right) \quad (2b)$$

129 The assumption that  $v_{\perp} = 0$  neglects ice flow parallel to topographic contours. It should be borne in  
 130 mind that contour lines do not always run perpendicular to valley walls, but are concave or convex  
 131 depending on location on the glacier. Contour-parallel flow could result in a non-stationary effect but it  
 132 is small on the scale of several ice thicknesses, and due to the low surface gradient of Black Rapids  
 133 Glacier [e.g. *Truffer et al.*, 2001; *Shugar et al.*, 2010]. Solving for the surface parallel and normal  
 134 (emergence) components, we obtain, respectively:

$$135 \quad v_{\parallel} = \frac{v^{(A)}(\eta_{\perp} \cdot \eta_{LOS}^{(D)}) - v^{(D)}(\eta_{\perp} \cdot \eta_{LOS}^{(A)})}{(\eta_{\parallel} \cdot \eta_{LOS}^{(A)})(\eta_{\perp} \cdot \eta_{LOS}^{(D)}) - (\eta_{\parallel} \cdot \eta_{LOS}^{(D)})(\eta_{\perp} \cdot \eta_{LOS}^{(A)})} \quad (3a)$$

$$136 \quad v_{\perp} = \frac{v^{(D)}(\eta_{\parallel} \cdot \eta_{LOS}^{(A)}) - v^{(A)}(\eta_{\parallel} \cdot \eta_{LOS}^{(D)})}{(\eta_{\parallel} \cdot \eta_{LOS}^{(A)})(\eta_{\perp} \cdot \eta_{LOS}^{(D)}) - (\eta_{\parallel} \cdot \eta_{LOS}^{(D)})(\eta_{\perp} \cdot \eta_{LOS}^{(A)})} \quad (3b)$$

137 Two descending-pass C-band ( $\lambda=0.056$  m) ERS-1/2 tandem images from 8 and 9 October 1995, and two  
 138 ascending-pass images from 11 and 12 October 1995 were used in this study (Table 1). The period  
 139 spanned by these tandem images is one day (24:00 hours).

140 Possible errors in the InSAR data are difficult to quantify. For displacement calculations, InSAR is  
 141 much more accurate than speckle tracking, thus most of the error derives from upscaling the error of the  
 142 one-day tandem acquisitions to an annual equivalent. Random errors were considerably reduced by  
 143 averaging to the lower spatial resolution of the speckle tracking (420 m x 315 m, see below). Systematic  
 144 errors from residual atmospheric phase will, however, be amplified by upscaling from one day to one  
 145 year. For the present study it is sufficient to state that the error of the InSAR-derived velocity maps is  
 146 smaller than that of the velocity maps derived from speckle tracking over annual periods (see below).  
 147 Local errors in ice flow direction derived from the digitization and interpolation of flow vectors are  
 148 estimated to be generally less than 2 degrees, which corresponds to a maximum 2% change in the  
 149 surface-parallel velocity. Corresponding errors in the surface-perpendicular velocity are augmented by  
 150 the smaller values of the perpendicular velocity.

### 151 3.2 Speckle tracking velocity measurements

152 If local phase shift gradients are too large due to rapid ice motion (more than one fringe per pixel), or  
153 random due to redistribution of snow, surface melt, or both, the phase can become decorrelated. As a  
154 result, the long temporal baselines of most spaceborne SAR systems result in generally poor phase  
155 correlation over temperate glaciers. A complementary approach to InSAR that overcomes this problem  
156 is speckle tracking. This method generates registration offsets between two SAR images in both slant  
157 range (satellite line-of-sight) and azimuth (parallel-to-satellite orbit) to map displacements [*Michel and*  
158 *Rignot, 1999; Gray et al., 2001; Werner et al., 2001; Strozzi et al., 2008*]. SAR intensity images are  
159 Fourier transformed, yielding the cross-correlation peak in pixel units [*Michel and Rignot, 1999*], and  
160 the image offset. Vertical velocity is ignored with speckle tracking, but it is safe to assume that the  
161 vertical component of the velocity is much smaller than the horizontal component.

162 Although less accurate than InSAR, radar speckle tracking has several advantages. The offset values  
163 are unambiguous 2D velocity measurements and do not require phase unwrapping, which can be  
164 difficult in steep mountains [*Shugar et al., 2010*] or for areas of fast ice flow [*Short and Gray, 2004*].  
165 When InSAR phase becomes decorrelated so does the speckle pattern between the images in each pair.  
166 However, speckle tracking may still find meaningful offsets by tracking macroscopic features (edges,  
167 ridges, crevasses) even in the complete absence of speckle correlation. In other words, there is a  
168 transition between speckle tracking and feature tracking.

169 The speckle tracking technique is accurate to  $\sim 0.05$  pixels [*Werner et al., 2001; Murray et al., 2002*],  
170 which corresponds to approximately 40 cm for a pixel size of 8 m (RADARSAT-1 Fine Mode). This  
171 amount is equivalent to 24 days of flow at  $1.7 \text{ cm d}^{-1}$  or a year of flow at  $0.1 \text{ cm d}^{-1}$ . In the present study,  
172 speckle tracking measurements on stationary features in the Delta River valley east of Black Rapids  
173 Glacier using annual Radarsat-1 image pairs gave an average displacement error of  $0.2 \text{ cm d}^{-1}$ , or  $\sim 0.1$   
174 pixels. In comparison, one-day repeat (ERS tandem) interferograms measure range displacements to a  
175 small fraction of the radar wavelength, down to 1 mm accuracy assuming prior compensation for the

176 atmospheric error. To directly compare the speckle tracking and InSAR results in this study, we spatially  
177 averaged all velocity data over a series of image subsets (chips), each equivalent to 420 x 315 m on the  
178 ground.

179 We computed velocity maps of Black Rapids Glacier in the vicinity of the landslides using 27 C-  
180 band ( $\lambda=0.056$  m) RADARSAT-1 images acquired during the melt seasons of 2003 to 2007 and four L-  
181 band ( $\lambda=0.236$  m) ALOS Palsar images from the melt season of 2007 (Table 1). We determined offsets  
182 for consecutive monthly scenes (e.g. 4 July and 28 July 2005) and annual pairs (e.g. 28 July 2005 and 23  
183 July 2006). We were thus able to quantify the glacier's seasonal velocity pattern, as well as the longer-  
184 term changes over the years following the earthquake and landslides.

### 185 **3.3 Ice dynamics modeling**

186 We used an ice-dynamics model employing the finite element method to understand the response of  
187 a glacier to rock avalanche debris cover. The model solves the full Stokes equations in the Lagrangian  
188 formulation, which contain longitudinal stress coupling; we used a Weertman-type sliding law enforced  
189 iteratively through a Dirichlet boundary condition. The model was constructed in Matlab employing the  
190 finite element method implementation of COMSOL Multiphysics. We use default P2-P1 elements for  
191 the velocity and linear elements for the pressure, and stabilized by streamline diffusion and crosswind  
192 diffusion [*Comsol*, 2008].

193 The DEM produced by *Shugar et al.* [2010] provides a 1995 surface elevation profile of Black  
194 Rapids Glacier along its centerline. However, values for ice thickness and thus bed elevation are  
195 published for only a few discrete locations. *Gades* [1998, see his Figure 4.6] produced an ice-thickness  
196 map by interpolating cross-glacier echo sounding profiles collected about every 2 km between about km  
197 6.5 and km 20. Other ice-thickness data were acquired along transverse ground penetrating radar (GPR)  
198 profiles that are unevenly spaced between km 14 and the terminus, with a maximum of about 4.9 km  
199 between profiles [*Heinrichs et al.*, 1995, their Figure 10]. Interpolation of point bed elevations gives a

200 bed profile with much less detail and accuracy than the surface profile. To produce a consistent pair of  
201 bed and surface elevation profiles, and to establish the glacier geometry at the time of the earthquake, we  
202 let the DEM surface evolve by running the full-Stokes model (see below) for several years, updating the  
203 surface elevation after each year by adding the difference between emergence velocity and local surface  
204 mass balance. The surface and bed of the two-dimensional flowband were then interpolated to an even  
205 50-m spacing using a spline. Net balance data used in the model come from mass balance measurements  
206 made over the past 40 years, and were scaled by the area-altitude distribution. This approach makes the  
207 simplifying assumption that centerline balances extend to the glacier margins [Arendt *et al.*, 2002; c.f.  
208 *Berthier et al.*, 2010]. The slope of the edge of the debris sheets was kept at or below the angle of repose  
209 (32 degrees). An adaptive triangular mesh was initially generated with 25-m spacing at the upper and  
210 lower boundaries. The mesh was then refined by a factor of approximately two with the “meshrefine”  
211 routine in Comsol. Figure 2 shows the model geometry, mass balance curve and mesh used to model ice  
212 flow with the finite element method.

213 Ice was treated as an incompressible non-Newtonian fluid with a rheology described by Glen’s flow  
214 law,  $\dot{\epsilon} = A\tau^n$ , with  $A = 2.4 \times 10^{-24} \text{ s}^{-1} \text{ Pa}^{-3}$  for temperate ice [Cuffey and Paterson, 2010] and  $n = 3$ . We  
215 used the 2D finite element method for the initial vertical flowband described above, to investigate if  
216 small changes in surface topography, slope, and mass balance are adequate to cause the velocity changes  
217 observed with satellites. The model implements a Weertman-style basal sliding law that includes  
218 effective water pressure as a Dirichlet boundary condition,  $v_B = \frac{k\tau_B^m}{p_{eff}}$ , where  $k$  is a sliding parameter  
219 ( $25 \text{ m a}^{-1} \text{ bar}^{-m}$ ),  $\tau_B$  is the basal shear stress, and  $m$  is a positive constant (2) [Bindschadler, 1983]. The  
220 value of  $m=2$  is within the range described by Bindschadler [1983] and provides a good fit to the SAR-  
221 derived velocity data. The effective pressure,  $p_{eff}$ , is the difference between the ice overburden pressure  
222 and water pressure. Water pressure was calculated as a fraction of ice overburden pressure, based on the  
223 piezometric surface described by Truffer *et al.* [2001, their Figure 8] of 55 m below the ice surface.

224 Lateral drag along valley walls is approximately taken into account via shape factor modification to the  
225 flow-law coefficient,  $A$  [Heinrichs *et al.*, 1996].

226 From the 2D finite element model, 1D curves of both surface-parallel and surface-perpendicular  
227 velocity can be calculated along the glacier surface. We verified the model against the Ice Sheet Model  
228 Intercomparison Project-Higher Order Models (ISMIP-HOM) benchmark using test data and  
229 experiments from Haut Glacier D’Arolla [Pattyn *et al.*, 2008].

230 Because bottom topography is poorly known, basal motion can only be roughly modeled in the full-  
231 Stokes model [Amundson *et al.*, 2006]. We made no attempt to model the inter-annual velocity  
232 fluctuations of Black Rapids Glacier, which are thought to be related to changes in basal conditions  
233 [Truffer and Harrison, 2006]. We also did not consider what is likely the complex influence of the Loket  
234 tributary on the flow of the main glacier trunk (Figure 1). We therefore do not expect our results to  
235 closely match observed velocities but rather we are more interested in recognizing characteristic spatio-  
236 temporal patterns of velocity and elevation change. By comparing modeled patterns of velocity change  
237 to measurements, we tried to understand whether the observed velocity fluctuations were mainly caused  
238 by the rock avalanches or, instead, were the result of the quiescent evolution of this surge-type glacier.

239 We ran two experiments to investigate the role of landslide debris on glacier velocity. In our control  
240 run, we allowed the glacier surface and velocity structure to evolve for five years (2002-2007) without  
241 any surface debris, thus simulating the evolution of the glacier without a landslide. Landslide deposition  
242 was then separately simulated by locally increasing  $h$  by the equivalent of a 2-m sheet of rock debris  
243 (bulk density  $2400 \text{ kg m}^{-3}$ ) over a horizontal distance of 7 km, between km 25 and km 32, which  
244 approximates the dimensions of the landslides on Black Rapids Glacier. The mass balance,  $b_m$ , under the  
245 debris-covered area was set to zero. The upper surface was iteratively updated according to the  
246 difference between mass balance and emergence velocity.

## 247 4 RESULTS

### 248 4.1 Ice velocity from SAR and ground surveys

249 Figure 3 shows the surface-parallel velocity field in the ablation area of Black Rapids Glacier in  
250 October 1995, obtained with SAR interferometry using ERS tandem data. The pattern and magnitudes of  
251 the velocity match those reported by *Fatland et al.* [2003] for January 1992 and December 1995, as well  
252 as survey velocities from 1995 (M. Truffer, personal communication, May 2011). The longitudinal  
253 velocity profile (Figure 3, inset) shows that the velocity just above the Locket tributary (km 23) is 50% of  
254 that between km 15 and km 20. The longitudinal velocity below the Locket tributary recovers to almost  
255 the values between km 15 and km 20. A second slowdown, smaller both spatially and in magnitude than  
256 that observed at the Locket tributary, occurs at about km 34, where a minor tributary joins Black Rapids  
257 Glacier. A velocity plateau is evident where another minor tributary joins the trunk glacier at km 30.

258 Five cross-glacier velocity profiles from the ablation area are also shown in Figure 3. The outer  
259 inflection points on each profile mark the transition from active to dead ice or moraine. The irregular  
260 form of profiles D and E reflects the influence of several minor tributaries and moraines.

261 The seasonal evolution of surface ice flow in the vicinity of the landslides is shown in Figures 4 and  
262 5. These results were obtained with the speckle tracking method using RADARSAT-1 and ALOS Palsar  
263 data. The velocity fields between 2003 and 2007 (Figure 5) are more variable and spatially  
264 heterogeneous than the velocity field in 1995 (Figure 3). Monthly velocities across BRG-west and BRG-  
265 middle (Figure 4A) are typically higher than across BRG-east, the lowest debris sheet. The highest  
266 seasonal velocities are in late May and June 2005 and in May and June 2007. Across chips 1-4 (see  
267 Figure 4A for locations of “chips”, or image subsets), which correspond to BRG-west and the upper half  
268 of BRG-middle, ice velocities ranged from around 23 cm d<sup>-1</sup> between late May and mid-June 2005, to  
269 around 19 cm d<sup>-1</sup> from mid-June to early July 2005. The upper margin of BRG-west had a velocity of  
270 nearly 22 cm d<sup>-1</sup> in June 2007, but the velocity decreases to 12 cm d<sup>-1</sup> in July of that year. By the end of

271 the melt seasons in 2003-2007, ice velocities were nearly the same (5-8 cm d<sup>-1</sup>) across the area covered  
272 by all three landslides.

273 Time series of surface ice flow rates derived from ground surveying, InSAR and radar speckle  
274 tracking (annual pairs) are shown in Figure 6. We calculated representative SAR-derived velocities  
275 across the debris sheet in spatially averaged chips and as point measurements for survey station km 29  
276 (Table 2). Figure 6A shows the mean velocity over the upglacier and downglacier chips of the debris  
277 sheet (chips 1 and 10, respectively), and the mean of all chips across the entire debris sheet (chips 1-10),  
278 averaged for each annual measurement in a particular melt season. Figure 6B shows the reduction in  
279 longitudinal velocity gradient with time, towards less compressional flow, from  $-5.7 \times 10^{-3} \text{ a}^{-1}$  in 1995 to  
280  $-4.1 \times 10^{-3} \text{ a}^{-1}$  in 2004 and only  $-1 \times 10^{-3} \text{ a}^{-1}$  in 2007.

281 Point velocities calculated by InSAR and optical surveying at stations km 20 and km 29 in 1995 are  
282 similar (Table 2). The mean 1995 InSAR-derived velocity across chips 1-10 is also similar to the  
283 surveyed ice velocity at km 29, which is located about halfway along this reach of the glacier. Despite  
284 an acceleration between 1995 and 1997 (Figure 6A), surveyed velocities at km 20 (Figure 6A) were the  
285 same in 1995 and 2002, before the earthquake. Similarly, the surveyed velocities at km 29 are about the  
286 same in 1995 and 2002. We thus infer that the mean velocity in the vicinity of the landslide debris  
287 immediately before the earthquake was approximately equal to the mean InSAR velocity for 1995  
288 (Figure 6A).

289 The annual surveyed velocities above the landslides (km 11, 14, and 20) show a short-lived, small  
290 acceleration (6-14%) in 2003, followed by a deceleration to values slightly less than in 2002 (Figure 6A).  
291 Survey data for 2009 show that the glacier was still slowing down at km 14 and km 20, although the  
292 exact velocity pattern at km 20 between 2005 and 2009 is unknown, because no survey measurement  
293 was made in 2007. We assume that velocity at km 20 is comparable to that measured at km 14, based on  
294 the similarity of the two series throughout the period of record.

295 The survey marker at km 29 was destroyed by one of the 2002 rock avalanches. Because the velocity  
296 pattern at km 29 is similar to that at km 20 between 1992 and 2002, we calculated an offset and  
297 projected the post-earthquake km 20 data to km 29 for 2007 (dashed continuation of km 29 line in  
298 Figure 6A). Using this approach, we estimated what the velocity at km 29 might have been in the  
299 absence of the landslides. The continued slowdown at km 29 in the absence of a landslide is supported  
300 by numerical modeling (see next section).

301 SAR speckle tracking measurements downglacier of km 20 reveal spatial and temporal velocity  
302 changes that appear too variable to be explained by natural evolution of the glacier, without the effect of  
303 the landslides. Notably, the measurements indicate a rapid increase in velocity by 2004. The mean SAR-  
304 derived velocity for the entire debris sheet in 2004 is 44% higher than the velocity derived from the  
305 2002 terrestrial surveying at km 29, which is located approximately in the middle of area covered by the  
306 debris sheet (Figure 6A, Table 2). The mean velocity in the area of the debris sheet decreases in each  
307 subsequent year at a greater rate than at survey sites higher on the glacier. Between 2004 and 2007, the  
308 mean velocity of the debris-covered ice decreased 30%, approaching the same velocity as measured by  
309 InSAR in 1995. Over the same period, ice velocity at site km 14 decreased by only 20%. In this context,  
310 the large velocity variations higher up on the glacier in the previous decades should be kept in mind.

311 The velocity of the upglacier margin of the debris (chip 1; open circles in Figure 6A) was the same  
312 in 1995 and 2004, as measured by SAR. Over the same period, the velocity of the downglacier margin of  
313 the debris sheet (chip 10; asterisks in Figure 6A) increased 109%. Between 2005 and 2007, the velocity  
314 of chip 10 continued to increase (Figure 6A), while the velocity of the downglacier half of the debris  
315 sheet decreased slightly.

316 The spatial pattern of velocity also changed after the landslides in 2002. In 1995, prior to landslide  
317 deposition, the velocity pattern could be characterized as generally decreasing towards the terminus,  
318 with significant decreases due to influences from tributary glaciers (Figure 3). Radar speckle tracking  
319 from 2004 until 2007, records progressive downglacier increases in ice velocity and a generally more

320 spatially heterogeneous velocity pattern (Figure 5). The highest recorded annual velocity ( $\sim 22 \text{ cm d}^{-1}$ ; 17  
321 May 2005 to 12 May 2006) is at chip 6 at the downglacier margin of BRG-middle.

## 322 4.2 Ice velocity from finite element model

323 In our model control run with no landslide debris (Figure 7), surface velocities decrease slightly over  
324 much of the glacier between 2002 and 2007, because the driving stress is reduced, mostly by thinning.  
325 The differences are greatest around km 20, which experiences a reduction of velocity of about 9%.  
326 Below km 30, there is little change in velocity over the five-year period, whereas above km 5, the  
327 velocity increases slightly due to thickening of the glacier.

328 Between km 25 and km 32, the main area of interest in this study, flow is compressional in 2002 ( $-$   
329  $2.9 \times 10^{-3} \text{ a}^{-1}$ ) and changes only slightly with time ( $-2.6 \times 10^{-3} \text{ a}^{-1}$  in 2007) in the control run. Between  
330 km 25 and km 28.5, which corresponds to the upglacier half of the area covered by landslide debris, the  
331 mean ice velocity without debris is consistently about  $3 \text{ cm d}^{-1}$  higher than between km 28.5 and km 32  
332 (Figure 7E).

333 After adding a debris sheet between km 25 and km 32 in the model, the upglacier end of the debris  
334 slows and the downglacier end accelerates, resulting in a switch from compressional to locally  
335 extensional flow by 2005 (Figure 7B, F). The velocity gradient between km 25 and km 32 changes from  
336  $-2.9 \times 10^{-3} \text{ a}^{-1}$  in 2002 (compressional flow) to  $2.0 \times 10^{-3} \text{ a}^{-1}$  in 2007 (extensional flow). At km 25, the ice  
337 velocity decreases 27% between 2002 and 2007; in contrast at km 32, the velocity increases 56% over  
338 the same period. Much of the change in total velocity can be explained by changes in basal motion  
339 (Figure 7D). For example, at km 32, the modeled surface velocity in 2002 is  $\sim 9.9 \text{ cm d}^{-1}$ , with  $7.1 \text{ cm d}^{-1}$   
340  $^1$  coming from basal motion. By 2007 (with landslide debris), total motion increases to  $\sim 15.4 \text{ cm d}^{-1}$ ,  
341 with  $11.1 \text{ cm d}^{-1}$  due to basal motion and the remainder due to ice creep.

342 Figure 8 shows the changes in the full-Stokes modeled 2D centerline velocity profile with and  
343 without the debris sheet. If the glacier is not covered by a debris sheet, the velocity vectors change little

344 over five years (compare Figure 8A and 8B), and flow is primarily emergent. With the addition of debris  
345 however, the velocity becomes strongly submergent at the upglacier end of the debris sheet (Figure 8C),  
346 and slightly less emergent at the downglacier end due to locally extending flow across the debris sheet.

## 347 **5 DISCUSSION**

348 Post-landslide changes to the surface velocity field of Black Rapids Glacier in the vicinity of the  
349 rock avalanche debris sheets include a substantial, but short-lived initial speed-up followed by a gradual  
350 slowdown to pre-earthquake values (Figure 6). The velocity changes under the debris are more rapid and  
351 of a higher magnitude than changes higher on the glacier, which are discussed below. Superimposed on  
352 these trends is a reduction of the longitudinal velocity gradient in the area covered by the debris sheet –  
353 the velocity of the downglacier half of the debris sheet increases, while the velocity of the upglacier half  
354 decreases or remains constant. Notably, the entire debris-covered part of the glacier trends towards a  
355 uniform surface velocity over the period of observation due to a reduction of surface slope of the debris-  
356 covered ice.

357 *Gardner and Hewitt* [1990] noted a similar change from compressional to extensional flow  
358 following deposition of three large landslides on Bualtar Glacier. In the ten months following the  
359 landslides, ice near the leading edge of the debris sheet moved four times faster than ice near the trailing  
360 edge. In the following 13 months, however, this pattern reversed, with ice near the trailing edge moving  
361 twice as fast as that near the leading edge.

362 The ice surface velocity upglacier from the debris sheets on Black Rapids Glacier increased slightly  
363 between 2002 and 2003. We propose three possible explanations for this speed-up. First, it may not  
364 represent a change in ice velocity, but rather an offset on the Denali fault during the earthquake. Right-  
365 lateral offset near the terminus of Black Rapids Glacier was about 4 m (about 1 cm d<sup>-1</sup> equivalent)  
366 [*Haeussler et al.*, 2004]. However, elevated velocities were observed over two consecutive seasons  
367 (2002-2003 and 2003-2004) at several survey sites (e.g. km 11 and km 14), suggesting that earthquake

368 displacement is probably not the cause of the increase in speed. Second, a short-lived speed-up may  
369 have been caused by an earthquake-generated change in the subglacial plumbing system. Although  
370 many authors have examined relationships between ice velocity and water pressure [e.g. *Truffer and*  
371 *Iken*, 1998; *Kavanaugh and Clarke*, 2001; *Truffer and Harrison*, 2006], none to our knowledge has  
372 specifically examined a possible relationship between earthquake shaking and till failure by excess pore  
373 water pressures. The observed speed-up at km 8 (M. Truffer, personal communication, May 2011),  
374 which is not on the Denali fault, casts doubt on this explanation, although the possibility of longitudinal  
375 coupling between the Denali fault and the ice at km 8 does not necessarily preclude it. Third, the speed-  
376 up may be associated with the decadal-scale oscillations noted earlier. *Nolan* [2003] reports that velocity  
377 oscillations during the quiescent phase of the glacier have a period of about 12 years. The velocity  
378 increase in 2002-2004 is smaller and has a shorter onset phase than that of the ~1992-2001 cycle, which  
379 itself is smaller and shorter than the first recorded cycle from ~1980 to 1992. The rapid termination and  
380 small magnitude of the most recent oscillation may be indicative of a trend towards more temporally  
381 constant flow. With only two or possibly three such oscillations, however, this argument is tenuous.  
382 Regardless, the speed-up recorded by surveys at km 8, 11, 14, and 20 is small and likely unrelated to the  
383 much larger speed-up of the debris-covered ice between km 25 and km 32 identified with the SAR  
384 speckle tracking.

385 Several authors [*Gordon et al.*, 1978; *Shulmeister et al.*, 2009] have suggested that landslide debris  
386 may alter glacier flow. The bulk density of rock avalanche debris is probably about  $2400 \text{ kg m}^{-3}$  [*Vacco*  
387 *et al.*, 2010], equivalent to about 2.6 m of ice-equivalent for every meter of debris. In the case of thin  
388 glaciers, an additional few meters of rock debris may increase the driving stress sufficiently to cause the  
389 glacier to speed-up by changing the deformational velocity alone. Black Rapids Glacier, however, is  
390 more than 450 m thick in the area of the landslides, and a few meters of rock debris alone is unlikely to  
391 alter the velocity significantly. A simple calculation of deformational velocity,

392  $v = \frac{2A}{(n+1)} (\rho g \sin \alpha)^n h^{(n+1)}$ , where  $\rho$  is ice density (917 kg m<sup>-3</sup>),  $g$  is gravitational acceleration (9.8 m  
393 s<sup>-2</sup>),  $\alpha$  is the glacier surface slope, and  $h$  is ice thickness (450 m), shows that an increase in ice thickness  
394 equivalent to 2 m of rock debris would result in less than a five percent increase in deformational  
395 velocity. More important factors are changes in mass balance resulting from strongly reduced ablation  
396 beneath the debris, changes in the vertical velocity under the debris resulting from a change to extending  
397 flow, and changes in the surface slope of the glacier. Changes in slope result from differential ablation at  
398 the upglacier and downglacier margins of the debris sheet and greater emergence velocities at the  
399 downglacier end than at the upglacier end. Both of these effects pivot the glacier surface towards the  
400 horizontal. In addition, steep ice cliffs develop at the upglacier and downglacier margins of the debris  
401 sheet due to the differential ablation. During fieldwork in 2007, the upglacier end of the 2-m-thick BRG-  
402 west debris sheet was perched on a pedestal of ice about 15 m high that dipped upglacier. The  
403 downglacier end of the BRG-west debris sheet similarly rested on a pedestal about 15 m high, but  
404 dipping downglacier. Thus the surface slope at the upglacier end was reversed, whereas the slope at the  
405 downglacier end was steeper than in 2002. An increase in ice thickness of 20 m, equivalent to 15 m of  
406 unmelted ice and 2 m of rock avalanche debris, results in nearly a 20% increase in velocity.

407 In our full-Stokes model (Figures 7, 8), the upglacier end of the debris sheet slows while the  
408 downglacier end speeds up in response to changes in surface slope and ice thickness. The emergence  
409 velocity adjusts to the switch from compressive flow in the ablation area to locally extending flow over a  
410 horizontal distance of 7 km. Basal velocity (Figure 7D), which is largely governed by surface slope in  
411 the Weertman-style sliding law used here, is reduced at the upglacier end of the debris sheet where a  
412 slope reversal occurs due to reduced or no ablation under the debris. Conversely, basal velocity at the  
413 downglacier margin of the debris increases due to a steep ice cliff caused by differential ablation. The  
414 qualitative match between the model results and the SAR-derived velocities indicates that the modeled  
415 scenario is a reasonable representation of the short-term evolution of the surface velocity of a glacier

416 covered by landslide debris. A shortcoming of our model is that we do not explicitly consider subglacial  
417 hydrology, even though changes in plumbing beneath a glacier, due for example to drainage of a  
418 supraglacial lake [*Sturm and Cosgrove, 1990*], certainly have an effect on surface motion.

419 The spatial velocity pattern observed with SAR speckle tracking at Black Rapids Glacier (Figure  
420 4A) is more complex than the model would suggest. In spring 2007, the velocity across the BRG-west  
421 debris sheet was very high ( $>20 \text{ cm d}^{-1}$ ) while the velocity across the BRG-east debris sheet was much  
422 lower ( $<6 \text{ cm d}^{-1}$ ). By early summer of 2007, surface velocities were much more uniform across all three  
423 debris sheets ( $\sim 10 \text{ cm d}^{-1}$ ). The short-lived acceleration at the upglacier end of the debris sheets may be  
424 related to the introduction of meltwater to the basal plumbing system from drainage of a supraglacial  
425 lake. Remote sensing data show that a supraglacial lake forming in spring 2007, dammed by the  
426 upglacier margin of the BRG-west debris sheet. The lake had mostly drained by mid-July 2007 (Figure  
427 9). In the 24 June 2007 RADARSAT-1 image, the lake was approximately 140 m wide and 840 m long.  
428 Assuming a constant glacier surface slope of  $2^\circ$  we estimate that the lake contained a minimum of  $\sim 2.9 \times$   
429  $10^5 \text{ m}^3$  of water. By 18 July, the lake contained only  $\sim 1.5 \times 10^4 \text{ m}^3$  of water. The lake is not visible on  
430 the 7 May or 31 May SAR images, but the reflectance of the pixels is very low, indicating a surface  
431 saturated with meltwater. During fieldwork in summer 2007, we observed the last remnant of the lake  
432 (Figure 9D), as well as a moulin about 3 m in diameter at the upglacier margin of the lake. The moulin  
433 drained the much larger lake earlier in the melt season.

434 The highest velocities measured by speckle tracking in 2007 occurred between 31 May and 24 June;  
435 the lowest velocities occurred in early autumn. We suggest that slow leakage from the supraglacial lake  
436 in May and June 2007 kept water pressure high, leading to low effective pressure, and enhanced basal  
437 sliding. In late June, the lake drained through one or more moulins, perhaps creating an efficient tunnel  
438 system, with a concomitant reduction in basal sliding and thus surface speed. This ice dynamics scenario  
439 is similar to that described for outburst floods at Kennicott Glacier. Several authors [*Anderson, S P et al.,*  
440 *2003; Anderson, R S et al., 2005; Bartholomaus et al., 2008*] have found that subglacial jökulhlaups

441 from Hidden Creek Lake have overpressurized the efficient conduit system, forcing water into an  
442 inefficient linked cavity system. The resulting high subglacial water pressures cause temporary bed  
443 separation and enhanced basal motion. Once the subglacial conduit system evolves to greater efficiency,  
444 the augmented basal motion ceases.

445 *Truffer et al.* [2005] noted that the low ice velocities measured at km 8 and km 14 on Black Rapids  
446 Glacier in 2004, which are some of the lowest in 32 years of record, are likely the result of an efficient  
447 water drainage network established at times of high runoff. *Meier et al.* [1994] described “extra-  
448 slowdown” events at Columbia Glacier in Alaska, when, after a speed-up event caused by enhanced  
449 input of water to the bed, the glacier slowed, ultimately reaching a velocity that was lower than that  
450 before the speed-up. Rapid transfer of a significant volume of water from a supraglacial lake to the  
451 glacier bed may have a similar effect at Black Rapids Glacier. Drainage of a supraglacial lake, however,  
452 is not a necessary precursor to a spring speed-up – Black Rapids Glacier is temperate-based, thus high  
453 water pressures can be expected whenever the basal drainage system is inefficient.

454 Alternatively, the spring speed-up may be caused by a hydraulic barrier at the bed, instigated by the  
455 reversed surface slope at the upglacier end of the rock avalanche debris. If large enough, this surface  
456 bulge could change the hydraulic potential gradient, causing a subglacial water pocket to form, which  
457 could lead to partial decoupling of the glacier from the bed. A lake drainage as discussed above, could  
458 then help drain the water pocket through an efficient pathway.

## 459 **6 CONCLUSIONS**

460 This study reports the impacts of three concurrent earthquake-triggered landslides on the behavior of  
461 Black Rapids Glacier. Observations and numerical modeling suggest that Black Rapids Glacier  
462 responded to a landslide-induced shut down of ablation by reducing the local velocity gradient.  
463 Surveying above the landslide debris sheets indicates a small acceleration of the glacier immediately  
464 after the earthquake (2002-2004) and a widespread slowdown thereafter. InSAR and satellite radar

465 speckle tracking (2003-2007) show a large increase in velocity in the area of the landslide debris sheets,  
466 especially at the downglacier end of the lowest debris sheet, where velocities nearly doubled. A full-  
467 Stokes, numerical ice-flow model produced similar results, suggesting that changes to mass balance,  
468 surface slope and a switch from compressional to extensional flow are responsible for the observed  
469 changes in surface velocity.

## 470 **7 ACKNOWLEDGEMENTS**

471 This research was funded through a Natural Sciences and Engineering Research Council of Canada  
472 (NSERC) Discovery Grant to Clague, a Canon National Parks Science Scholarship to Capps, and an  
473 NSERC-PGS-D3 Scholarship, Geological Society of America Bruce ‘Biff’ Reed Research Grant,  
474 Northern Scientific Training Programme grants and an Arctic Institute of North America Grant-in-Aid to  
475 Shugar. The European Space Agency supplied ERS data (Category-1 proposal No. 3970); Macdonald  
476 Dettwiler and Associates and UNAVCO provided the RADARSAT data free of charge. We thank M.  
477 Truffer and M. Stuefer, amongst many others, who maintain the currently unfunded effort of ground  
478 surveying at Black Rapids Glacier. We also thank E. Pettit and the US Army (Fort Wainwright, Alaska)  
479 for logistical support, and Marmot Mountain Canada for generous in-kind support. This contribution  
480 benefited greatly from conversations with G. Flowers. Suggestions by M. Lüthi, two anonymous  
481 reviewers, Editor A. Densmore and Associate Editor M. Truffer greatly strengthened the paper.

482  
483  
484  
485

## **8 REFERENCES**

- 486 Amundson, J. M., M. Truffer, and M. P. Luthi (2006), Time-dependent basal stress conditions beneath  
487 Black Rapids Glacier, Alaska, USA, inferred from measurements of ice deformation and surface motion,  
488 *J. Glaciol.*, 52, 347-357.
- 489 Anderson, R. S., J. S. Walder, S. P. Anderson, D. C. Trabant, and A. G. Fountain (2005), The dynamic  
490 response of Kennicott Glacier, Alaska, USA, to the Hidden Creek Lake outburst flood, *Ann. Glaciol.*, 40,  
491 237-242.
- 492 Anderson, S. P., J. S. Walder, R. S. Anderson, E. R. Kraal, M. Cunico, A. G. Fountain, and D. C.  
493 Trabant (2003), Integrated hydrologic and hydrochemical observations of Hidden Creek Lake  
494 jokulhlaups, Kennicott Glacier, Alaska, *J. Geophys. Res.-Earth Surf.*, 108.

- 495 Arendt, A. A., K. A. Echelmeyer, W. D. Harrison, C. S. Lingle, and V. B. Valentine (2002), Rapid  
496 wastage of Alaska glaciers and their contribution to rising sea level, *Science*, 297, 382-386.
- 497 Bartholomaeus, T. C., R. S. Anderson, and S. P. Anderson (2008), Response of glacier basal motion to  
498 transient water storage, *Nature Geosci.*, 1, 33-37.
- 499 Berthier, E., E. Schiefer, G. K. C. Clarke, B. Menounos, and F. Remy (2010), Contribution of Alaskan  
500 glaciers to sea-level rise derived from satellite imagery, *Nature Geosci.*, 3, 92-95.
- 501 Bindschadler, R. (1983), The importance of pressurized subglacial water in separation and sliding at the  
502 glacier bed, *J. Glaciol.*, 29, 3-19.
- 503 Bull, C., and C. Marangunic (1967), The earthquake-induced slide on the Sherman Glacier, south-central  
504 Alaska, and its glaciological effects, paper presented at Physics of Snow and Ice; International  
505 Conference on Low Temperature Science, Sapporo, Japan.
- 506 Bull, C., and C. Marangunic (1968), Glaciological effects of debris slide on Sherman Glacier, in *The  
507 Great Alaska Earthquake of 1964 - Hydrology, Pt. A*, pp. 309-317, National Academy of Sciences,  
508 Washington, D.C.
- 509 Comsol (2008), COMSOL Multiphysics Reference Guide 3.5A, Burlington, MA.
- 510 Cuffey, K. M., and W. S. B. Paterson (2010), *The Physics of Glaciers*, 4th ed., 693 pp., Butterworth-  
511 Heinemann, Boston, MA.
- 512 Deline, P. (2005), Change in surface debris cover on Mont Blanc massif glaciers after the 'Little Ice Age'  
513 termination, *Holocene*, 15, 302-309.
- 514 Fatland, D. R., C. S. Lingle, and M. Truffer (2003), A surface motion survey of Black Rapids Glacier,  
515 Alaska, USA, *Ann. Glaciol.*, 36, 29-36.
- 516 Fischer, U. H., A. Braun, A. Bauder, and G. E. Flowers (2005), Changes in geometry and subglacial  
517 drainage derived from digital elevation models: Unteraargletscher, Switzerland, 1927-97, *Ann. Glaciol.*,  
518 40, 20-24.
- 519 Fountain, A., and B. H. Vaughan (1995), Changing drainage patterns within South Cascade Glacier,  
520 Washington, USA, 1964-1992, paper presented at Biogeochemistry of Seasonally Snow-Covered  
521 Catchments, International Association of Hydrological Sciences Publication 228, Boulder, CO.
- 522 Gades, A. (1998), Spatial and temporal variations of basal conditions beneath glaciers and ice sheets  
523 inferred from radio echo sounding measurements, Ph.D. thesis, 192 pp, University of Washington,  
524 Seattle.
- 525 Gardner, J. S., and K. Hewitt (1990), A surge of Bualtar Glacier, Karakoram Range, Pakistan - A  
526 possible landslide trigger, *J. Glaciol.*, 36, 159-162.
- 527 Geertsema, M., J. J. Clague, J. W. Schwab, and S. G. Evans (2006), An overview of recent large  
528 catastrophic landslides in northern British Columbia, Canada, *Eng. Geol.*, 83, 120-143.
- 529 Gordon, J. E., R. V. Birnie, and R. Timmis (1978), A major rockfall and debris slide on Lyell Glacier,  
530 South Georgia, *Arc. Alp. Res.*, 10, 49-60.

- 531 Gray, A. L., N. Short, K. E. Mattar, and K. C. Jezek (2001), Velocities and flux of the Filchner ice shelf  
532 and its tributaries determined from speckle tracking interferometry, *Can. J. Rem. Sens.*, 27, 193-206.
- 533 Gulley, J., and D. I. Benn (2007), Structural control of englacial drainage systems in Himalayan debris-  
534 covered glaciers, *J. Glaciol.*, 53, 399-412.
- 535 Haeussler, P. J., D. P. Schwartz, T. E. Dawson, H. D. Stenner, J. J. Lienkaemper, B. Sherrod, F. R. Cinti,  
536 P. Montone, P. A. Craw, A. J. Crone, and S. F. Personius (2004), Surface rupture and slip distribution of  
537 the Denali and Totschunda faults in the 3 November 2002 M 7.9 earthquake, Alaska, *Bull. Seism. Soc.*  
538 *Am.*, 94, S23-S52.
- 539 Hance, J. H. (1937), The recent advance of Black Rapids Glacier, Alaska, *J. Geol.*, 45, 775-783.
- 540 Harrison, W., L. Mayo, and D. Trabant (1975), Temperature measurements of Black Rapids Glacier,  
541 Alaska, paper presented at 24th Alaska Science Conference, University of Alaska Fairbanks, AK.
- 542 Heinrichs, T. A., L. R. Mayo, K. A. Echelmeyer, and W. D. Harrison (1996), Quiescent-phase evolution  
543 of a surge-type glacier: Black Rapids Glacier, Alaska, USA, *J. Glaciol.*, 42, 110-122.
- 544 Heinrichs, T. A., L. R. Mayo, D. Trabant, and R. March (1995), Observations of the surge-type Black  
545 Rapids Glacier, Alaska, during a quiescent period, 1970-92., in *U.S. Geol. Surv. Open File 94-512*, 131  
546 pp.
- 547 Joughin, I. R., R. Kwok, and M. A. Fahnestock (1998), Interferometric estimation of three-dimensional  
548 ice-flow using ascending and descending passes, *IEEE Trans. Geosci. Rem. Sens. Lett.*, 36, 25-37.
- 549 Kavanaugh, J. L., and G. K. C. Clarke (2001), Abrupt glacier motion and reorganization of basal shear  
550 stress following the establishment of a connected drainage system, *J. Glaciol.*, 47, 472-480.
- 551 Lang, O., B. T. Rabus, and S. W. Dech (2004), Velocity map of the Thwaites Glacier catchment, West  
552 Antarctica, *J. Glaciol.*, 50, 46-56.
- 553 Massom, R., and D. Lubin (2006), *Polar Remote Sensing: Volume II, Ice Sheets*, 426 pp.,  
554 Springer/Praxis, Chichester, UK.
- 555 Meier, M., S. Lundstrom, D. Stone, B. Kamb, H. Engelhardt, N. Humphrey, W. W. Dunlap, M.  
556 Fahnestock, R. M. Krimmel, and R. Walters (1994), Mechanical and hydrologic basis for the rapid  
557 motion of a large tidewater glacier 1. Observations, *J. Geophys. Res.*, 99, 15219-15229.
- 558 Michel, R., and E. Rignot (1999), Flow of Glaciar Moreno, Argentina, from repeat-pass Shuttle Imaging  
559 Radar images: Comparison of the phase correlation method with radar interferometry, *J. Glaciol.*, 45,  
560 93-100.
- 561 Mohr, J. J., N. Reeh, and S. N. Madsen (2003), Accuracy of three-dimensional glacier surface velocities  
562 derived from radar interferometry and ice-sounding radar measurements, *J. Glaciol.*, 49, 210-222.
- 563 Murray, T., T. Strozzi, A. Luckman, H. Pritchard, and H. Jiskoot (2002), Ice dynamics during a surge of  
564 Sortebrae, East Greenland, *Ann. Glaciol.*, 34, 323-329.
- 565 Nolan, M. (2003), The galloping glacier trots: decadal-scale speed oscillations within the quiescent  
566 phase, *Ann. Glaciol.*, 36, 7-13.

- 567 Pattyn, F., L. Perichon, A. Aschwanden, B. Breuer, D. de Smedt, O. Gagliardini, G. H. Gudmundsson, R.  
568 C. A. Hindmarsh, A. Hubbard, J. V. Johnson, T. Kleiner, Y. Kononov, C. Martin, J. A. Payne, D.  
569 Pollard, S. Price, M. Ruckamp, F. Saito, O. Soucek, S. Sugiyama, and T. Zwinger (2008), Benchmark  
570 experiments for higher-order and full-Stokes ice sheet models (ISMIP-HOM), *The Cryosphere*, 2, 95-  
571 108.
- 572 Péwé, T. L. (1951), Recent history of Black Rapids Glacier, Alaska, *Geol. Soc. Am. Bull.*, 62, 1558-1558.
- 573 Post, A. S. (1960), The exceptional advances of the Muldrow, Black Rapids, and Susitna Glaciers, *J.*  
574 *Geophys. Res.*, 65, 3703-3712.
- 575 Rabus, B. T., and D. R. Fatland (2000), Comparison of SAR-interferometric and surveyed velocities on  
576 a mountain glacier: Black Rapids Glacier, Alaska, USA, *J. Glaciol.*, 46, 119-128.
- 577 Rabus, B. T., and O. Lang (2000), Ice motion and topography in the Siachen Glacier area, central  
578 Kashmir, derived with an operational processing system for INSAR-DEMs, paper presented at Fringe  
579 '99: Advancing ERS SAR Interferometry from Applications towards Operations, European Space  
580 Agency, Liege, Belgium, 10-12 November 1999.
- 581 Reynolds, J. M. (2000), On the formation of supraglacial lakes on debris-covered glaciers, in *Debris-*  
582 *Covered Glaciers*, edited by M. Nakawo, C. F. Raymond and A. Fountain, pp. 153-161, IAHS-AISH  
583 Publication 264, Seattle, WA.
- 584 Reznichenko, N., T. Davies, J. Shulmeister, and M. J. McSaveney (2010), Effects of debris on ice-  
585 surface melting rates: an experimental study, *J. Glaciol.*, 56, 384-394.
- 586 Reznichenko, N., T. R. H. Davies, and D. J. Alexander (2011), Effects of rock avalanches on glaciers  
587 behaviour and moraines formation, *Geomorphology*, 132, 327-338.
- 588 Short, N. H., and A. L. Gray (2004), Potential for RADARSAT-2 interferometry: Glacier monitoring  
589 using speckle tracking, *Can. J. Rem. Sens.*, 30, 504-509.
- 590 Shugar, D. H., and J. J. Clague (in press), The sedimentology and geomorphology of rock avalanche  
591 deposits on glaciers, *Sedimentology*.
- 592 Shugar, D. H., B. T. Rabus, and J. J. Clague (2010), Elevation changes (1949-1995) of Black Rapids  
593 Glacier, Alaska, derived from a multi-baseline InSAR DEM and historical maps, *J. Glaciol.*, 56, 625-  
594 634.
- 595 Shulmeister, J., T. R. Davies, D. J. A. Evans, O. M. Hyatt, and D. S. Tovar (2009), Catastrophic  
596 landslides, glacier behaviour and moraine formation - A view from an active plate margin, *Quat. Sci.*  
597 *Rev.*, 28, 1085-1096.
- 598 Strozzzi, T., A. Kouraev, A. Wiesmann, U. Wegmuller, A. Sharov, and C. Werner (2008), Estimation of  
599 Arctic glacier motion with satellite L-band SAR data, *Rem. Sens. Env.*, 112, 636-645.
- 600 Sturm, M., and D. M. Cosgrove (1990), An unusual jökulhlaup involving potholes on Black Rapids  
601 Glacier, Alaska Range, Alaska, USA, *J. Glaciol.*, 36, 125-126.
- 602 Tarr, R. S. (1910), The theory of advance of glaciers in response to earthquake shaking, *Zeit. Fur*  
603 *Gletsch.*, 5, 1-35.

- 604 Truffer, M., K. A. Echelmeyer, and W. D. Harrison (2001), Implications of till deformation on glacier  
605 dynamics, *J. Glaciol.*, *47*, 123-134.
- 606 Truffer, M., and W. D. Harrison (2006), In situ measurements of till deformation and water pressure, *J.*  
607 *Glaciol.*, *52*, 175-182.
- 608 Truffer, M., W. D. Harrison, and R. S. March (2005), Record negative glacier balances and low  
609 velocities during the 2004 heatwave in Alaska, USA: Implications for the interpretation of observations  
610 by Zwally and others in Greenland, *J. Glaciol.*, *51*, 663-664.
- 611 Truffer, M., and A. Iken (1998), The sliding velocity over a sinusoidal bed at high water pressure, *J.*  
612 *Glaciol.*, *44*, 379-382.
- 613 Truffer, M., R. J. Motyka, W. D. Harrison, K. A. Echelmeyer, B. Fisk, and S. Tulaczyk (1999),  
614 Subglacial drilling at Black Rapids Glacier, Alaska, USA: Drilling method and sample descriptions, *J.*  
615 *Glaciol.*, *45*, 495-505.
- 616 Vacco, D. A., R. B. Alley, and D. Pollard (2010), Glacial advance and stagnation caused by rock  
617 avalanches, *Earth Plan. Sci. Lett.*, *294*, 123-130.
- 618 Werner, C., T. Strozzi, A. Wiesmann, U. Wegmuller, T. Murray, L. Pritchard, and A. Luckman (2001),  
619 Complimentary [sic] measurement of geophysical deformation using repeat-pass SAR, in *Proceedings*  
620 *of IGARSS 2001: Scanning the Present and Resolving the Future*, pp. 3255-3258.  
621  
622

623  
624  
625  
626  
627  
628  
629  
630  
631  
632  
633  
634  
635  
636  
637  
638  
639  
640  
641  
642  
643  
644  
645  
646  
647  
648  
649  
650  
651  
652  
653  
654  
655  
656  
657  
658  
659  
660  
661  
662  
663  
664  
665  
666  
667  
668  
669  
670  
671

## Figure Captions

Figure 1 (A). Map of Black Rapids Glacier showing the trace of the Denali Fault (dotted line), the three landslide debris sheets (dark grey shading), and distances from the head of the glacier in 5 km increments [modified from *Amundson et al.*, 2006, reprinted from the Journal of Glaciology with permission of the International Glaciological Society]. Delta River is shown with a wavy pattern. Locations of Fairbanks and Black Rapids Glacier are shown on the inset map with an open circle and star, respectively. (B). Photograph of the BRG-east debris sheet looking west. The BRG-middle debris sheet is in the background. Photo courtesy of Dennis Trabant (US Geological Survey).

Figure 2 (A) Glacier geometry, (B) net balance, and (C) mesh used in the ice dynamics model. Dashed box in (A) represents area shown in (C).

Figure 3 Surface-parallel velocity of Black Rapids Glacier in October 1995 overlain on a geocoded SAR amplitude image. The inset is a profile of ice velocity along the glacier centerline. The black strips are the locations of transverse velocity profiles, shown at the right. The ascending ERS scenes are restricted to the ablation area of the glacier; as a result the velocity map terminates just upstream of profile A at the bend near the equilibrium line. Dashed box outlines region of interest shown in panels in Figure 4. The Loket tributary enters the main trunk of Black Rapids Glacier around km 25, causing a reduction in surface velocity just above the confluence.

Figure 4 Black Rapids Glacier velocity field derived from RADARSAT-1 speckle tracking. (A) 31 May – 24 June 2007. (B) 11 August – 4 September 2007. Survey stations km 20, 26, 29, and 32 are shown in (A), along with chip outlines. Landslide debris sheets are outlined in yellow.

Figure 5 Twenty-four day leapfrog speckle tracking velocity fields for the period 2003-2007. (A) RADARSAT-1 speckle tracking maps in the vicinity of the rock avalanche debris sheets. Rock avalanche debris sheets are outlined with yellow dashed lines in bottom-right panel. (B) Average velocity at each debris sheet based on RADARSAT-1 and ALOS Palsar data.

Figure 6 Magnitude of surface ice velocity derived from ground surveying, InSAR, and speckle tracking. (A) Mean of uppermost and lowermost chips on debris-covered ice (chips 1 and 10). Solid lines record terrestrial surveying data; circles, dots, and asterisks represent SAR-derived velocities. (B) Longitudinal velocity gradient from 1995 to 2007 for the part of the glacier covered by landslide debris. The 1995 data point is an InSAR-derived velocity for October 1995, averaged over the same chips as for the speckle tracking (Figure 3) and converted to an annual equivalent velocity [*Rabus and Fatland*, 2000].

Figure 7 Modeled glacier velocities calculated using the full-Stokes model. Panels A and B show the horizontal surface velocity for, respectively, the control run and the run with landslide debris from km 25 to km 32. Panels C and D show the basal velocity for the control run and the landslide debris. Open circles in panels E and F show that the mean velocity from km 25 to km 28.5 (upglacier half of debris-covered area); asterisks show the mean velocity from km 28.5 to km 32 (downglacier half of debris-covered area); and the solid line represents the velocity gradient between km 25 and km 32. For clarity, model results are shown only for km 15 to km 40.

Figure 8 Centerline velocity profiles for (A) 2002 prior to landslide, (B) the 2007 control run (no landslide debris), and (C) the 2007 run with landslide debris cover. Arrows indicate velocity directions and represent only a small subset of the velocity vectors in the model. The model was run for the entire

672 40-km long glacier, as shown in Figure 2; for clarity, only the area covered by, or adjacent to, the  
673 landslide debris is shown here.

674

675 Figure 9 SAR images showing (A) a melting glacier surface on 31 May 2007, (B) a large lake upglacier  
676 of BRG-west on 24 June 2007, and (C) the much smaller, drained lake on 18 July 2007. (D) Photo  
677 collage of the lake on 8 July 2007. Glacier flows from left to right in all panels.

678

679

680

681

**Table 1 Details of radar satellite images used in this study.**

Sensor	Date (mm/dd/yyyy)	Spatial resolution (m)	Wavelength (cm)	Flight direction
ERS-1	10/08/1995	25	5.66	Descending ( $B_{\perp}$ = -302 m)
ERS-2	10/09/1995			
ERS-1	10/11/1995			
ERS-2	10/12/1995			
RADARSAT-1	06/21/2003	8	5.66	Descending
	07/15/2003			
	08/08/2003			
	09/01/2003			
	06/15/2004			
	07/09/2004			
	08/02/2004			
	08/26/2004			
	09/19/2004			
	05/17/2005			
	06/10/2005			
	07/04/2005			
	07/28/2005			
	08/21/2005			
	09/14/2005			
	05/12/2006			
	06/05/2006			
	07/23/2006			
	08/16/2006			
	09/09/2006			
05/07/2007				
05/31/2007				
06/24/2007				
07/18/2007				
08/11/2007				
09/04/2007				
09/28/2007				
ALOS Palsar	06/22/2007	10	23.6	Descending
	08/07/2007			
	07/09/2007			
	08/24/2007			

682

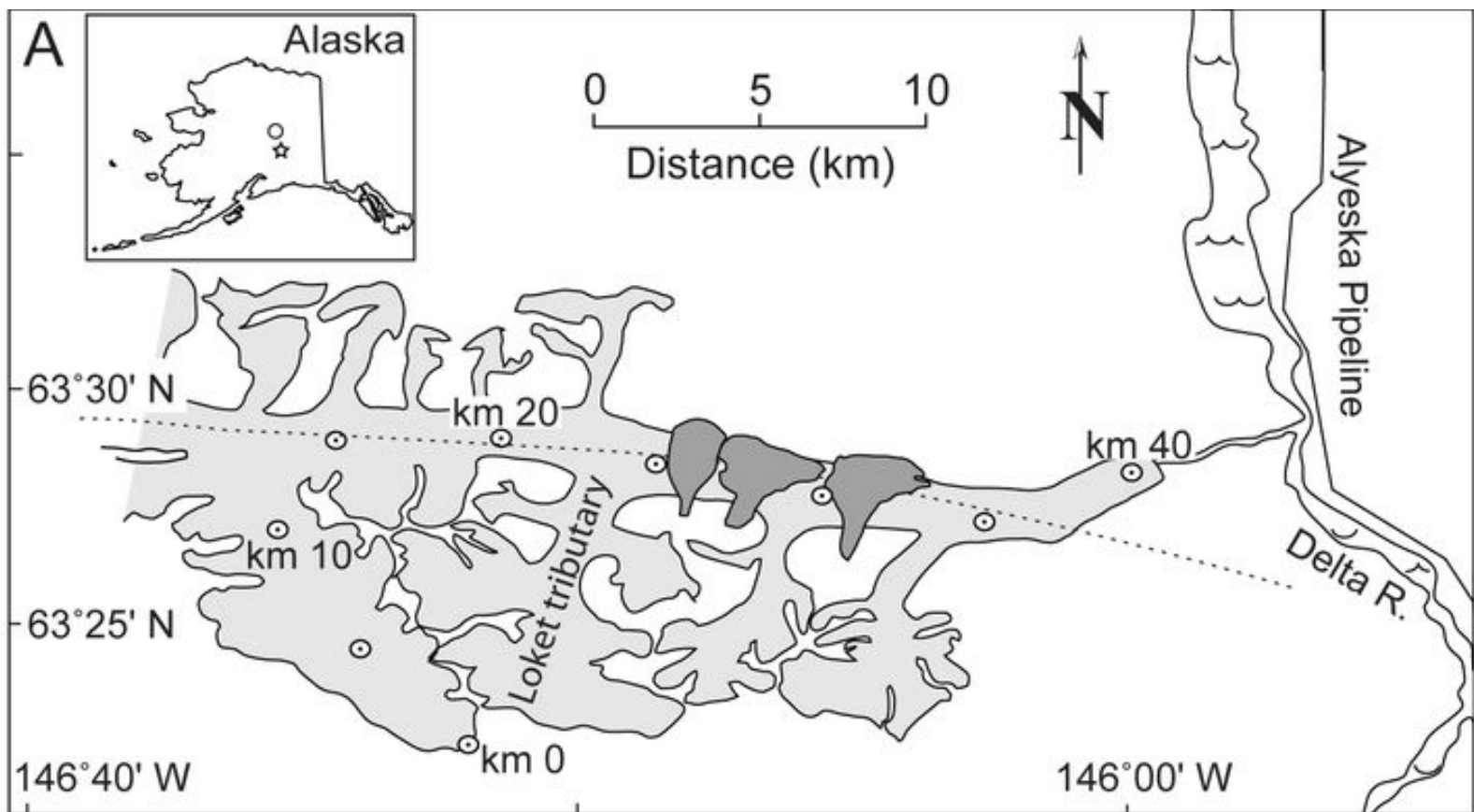
683

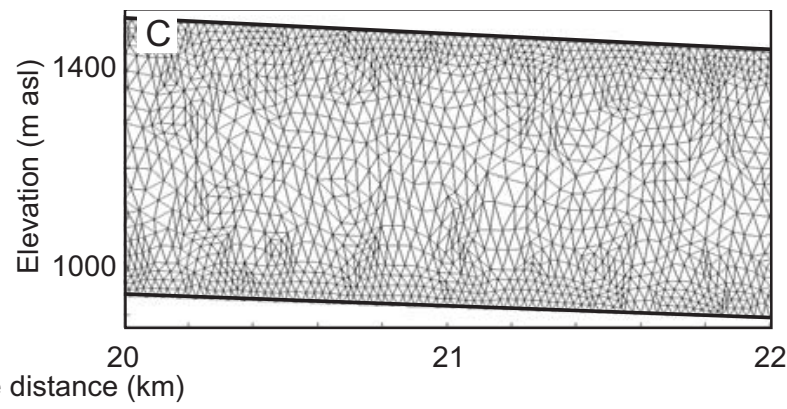
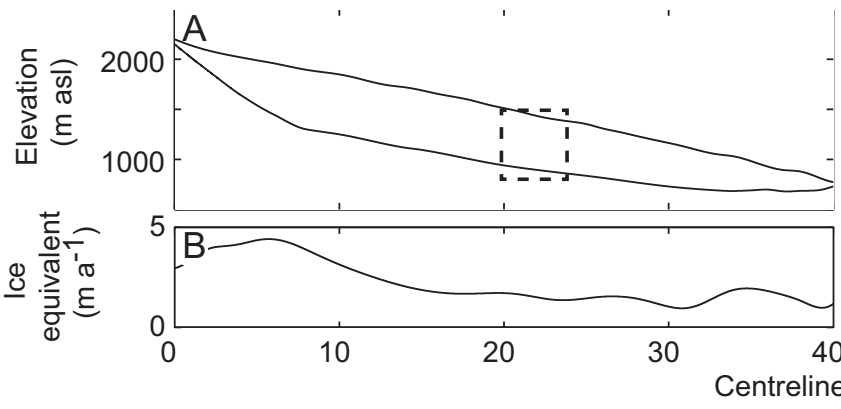
**Table 2 Surface velocities ( $\text{cm d}^{-1}$ ) measured by ground surveying, InSAR<sup>‡</sup> and radar speckle tracking<sup>¶</sup>.**

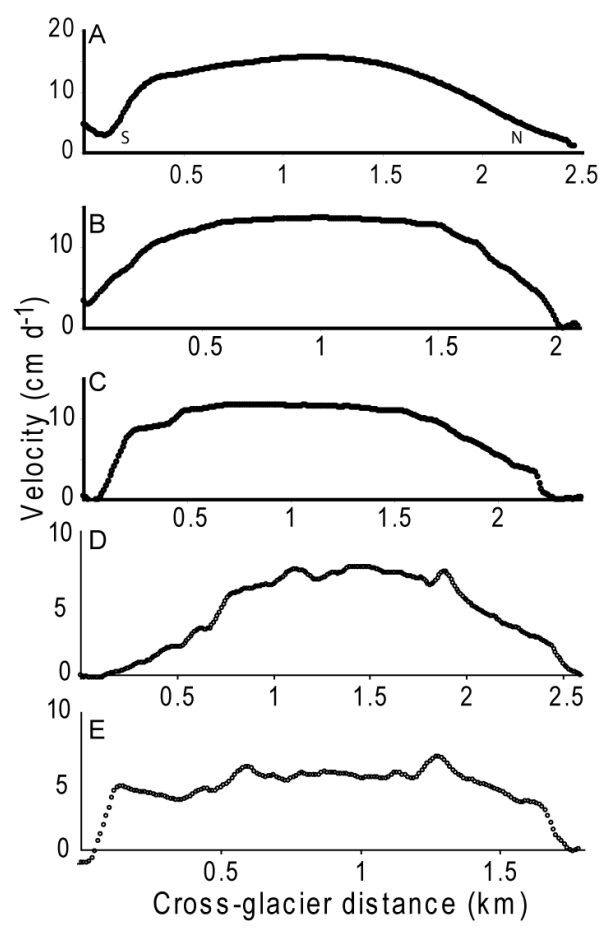
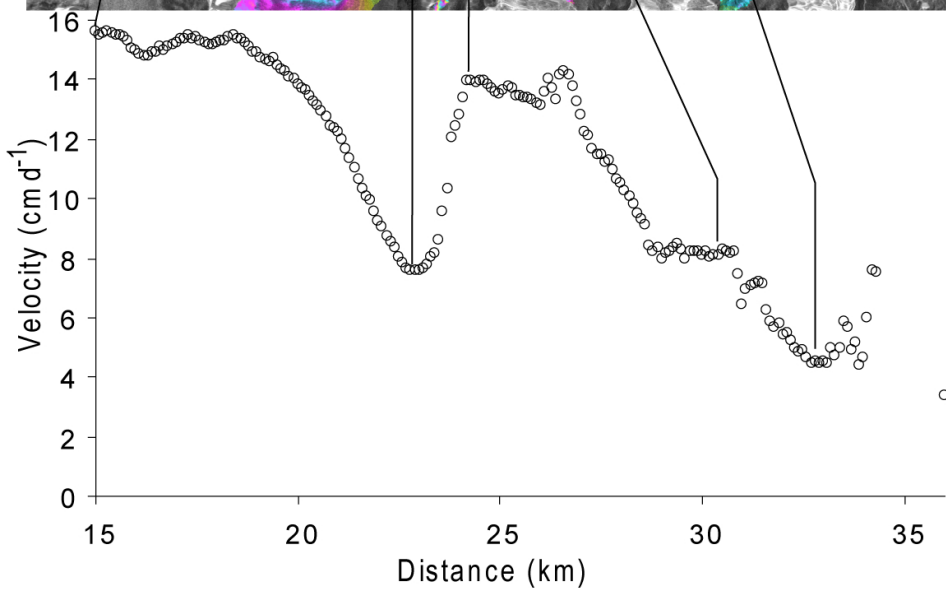
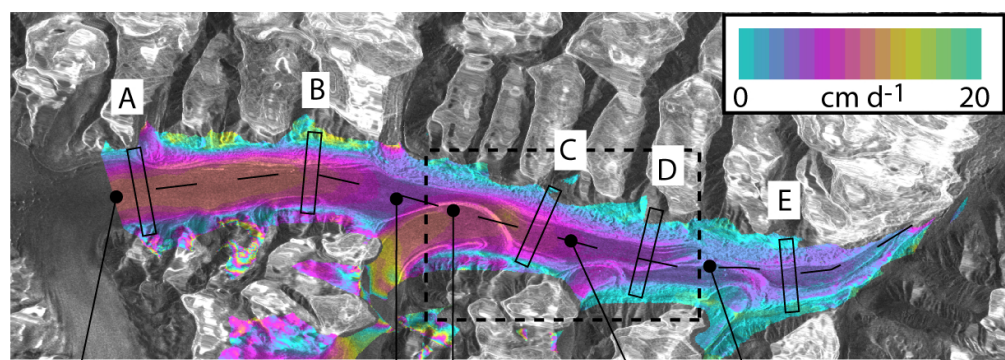
Location	Ground survey							SAR				
	1995	2002	2003	2004	2005	2007	2009	1995	2004	2005	2006	2007
km 11	20.2	20.3	22.2	21.9	18.3							
km 14	16.7	15.8	18.1	16.8	14.0	13.3	12.7					
km 20	14.2	14.2	15.1	13.2	13.2		10.6	13.8				
km 29	8.6	8.9						9.0	11.5	10.0	9.2	8.5
Chips 1-10								8.9	12.8	10.7	10.0	9.4
Chip 1								13.1	13.1	12.9	10.6	9.9
Chip 10								4.5	9.4	7.3	7.6	8.3

685 <sup>‡</sup>The InSAR data does not extend to the km 14 survey station – thus only stations km 20 and km29 are listed for 1995.686 <sup>¶</sup>The speckle tracking data have coherence only on the debris-covered ice; therefore we provide only a point measurement at  
687 survey station km 29.

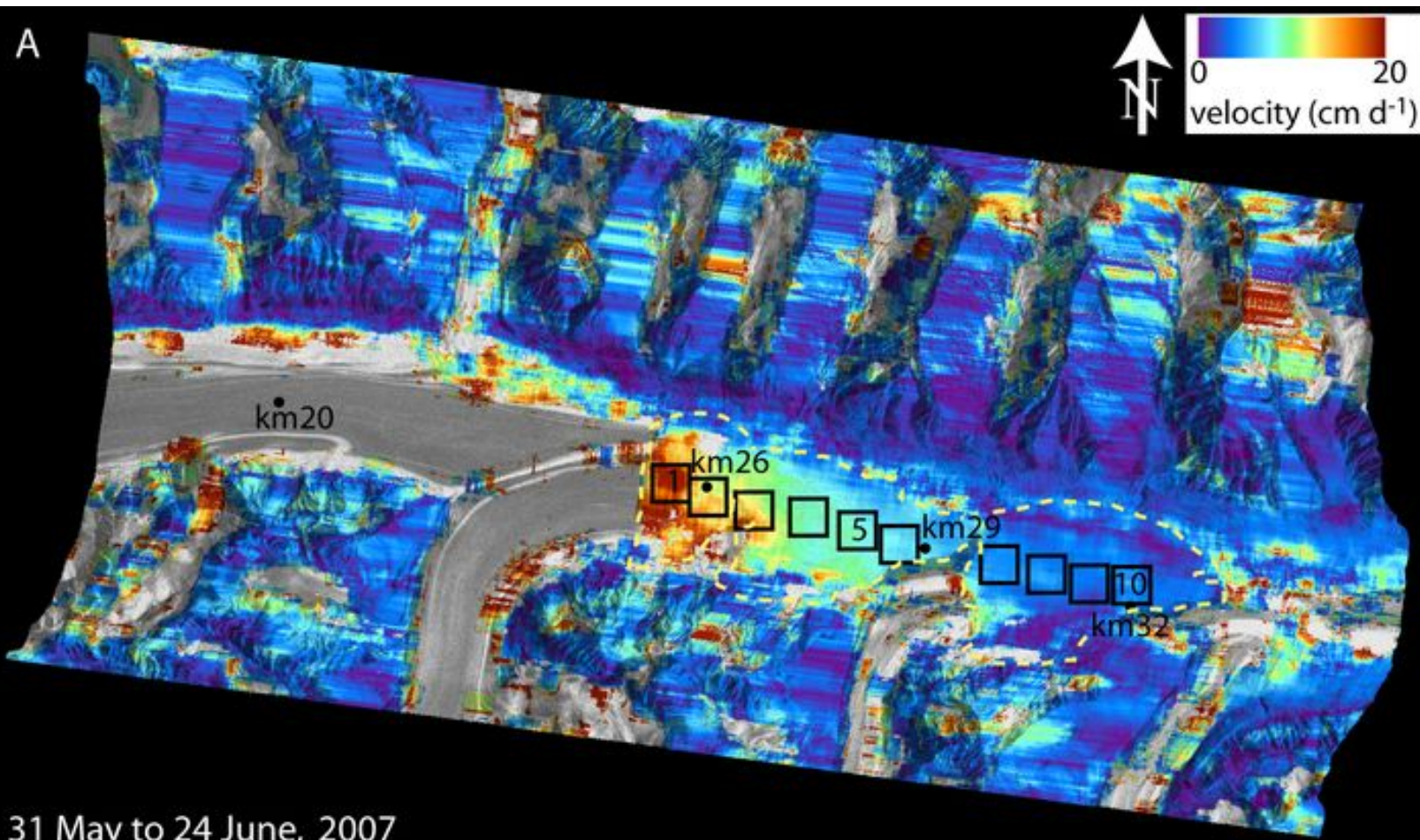
688







A



B

